Soil characterisation using a dynamic penetrometer

Junlin Rong[1#], and *Majidreza* Nazem[2]

[1] *Ph.D. Candidate, Department of Civil and Infrastructure Engineering, RMIT University, Melbourne, 3000, VIC, Australia*
[2] *Professor, Department of Civil and Infrastructure Engineering, RMIT University, Melbourne, 3000, VIC, Australia*
[#]*Corresponding author: junlin.rong@rmit.edu.au*

ABSTRACT

In offshore engineering, a geotechnical site investigation is an important step in analysis and design to ensure the integrity and serviceability of infrastructure. The Cone Penetration Test (CPT) stands as the prevailing technology for offshore soil characterisation. However, this test method requires a substantial allocation of resources for equipment transportation and operation personnel. This proves inefficient and costly for conducting comprehensive surveys over ocean beds. Alternatively, free-falling penetrometers (FFP) have attracted attention as a CPT replacement for soil characterisation. Nevertheless, these devices can penetrate only to shallow depths within soils, limiting their applicability for offshore site investigation purposes. A new device has been created to overcome this constraint, featuring a dynamic penetrometer launched by a speargun. Unlike conventional free-falling penetrometers, this apparatus can attain a greater penetration ratio, exceeding 20 times its diameter. The process of experimental testing yielded notable enhancements, particularly in effectively addressing challenges associated with tilting when attempting low-penetration depths. By implementing rate corrections into the methodology, promising results were obtained for equivalent static penetration resistance. This approach not only represents the capacity to influence future penetrometer designs but elevates the overall efficiency of in-situ soil characterisation procedures.

Keywords: dynamic penetration, offshore engineering, rate effect, sand.

1. Introduction

The cone penetration test (CPT) is used to determine the geotechnical engineering properties of soils and to delineate soil stratigraphy. The onshore CPT is well-established, and a fully equipped vehicle can effectively conduct the test. The test cannot be easily performed in inaccessible sites, such as the seabeds. This is primarily attributed to the high costs and labour-intensive nature associated with its deployment. On the other hand, dynamic penetrometers have been employed to provide information on the mechanical properties of the soil in the past few decades, such as free-falling penetrometers (FFP, Randolph et al. 2018). These devices can provide penetration data, including the total time and depth of penetration as well as the deceleration characteristic of the penetrometer, in order to infer soil properties.

The applications of FFP have been reported in both military and civilian tasks. Military purposes include naval mine countermeasures and terminal ballistic studies, extraterrestrial exploration, and deep-sea nuclear waste disposal. In civilian applications, FFPs have been used in the offshore oil and gas industry, such as determining the soil strength for pipeline feasibility investigations, anchoring systems, and dam and harbour health monitoring (Nazem et al. 2012; Chow and Airey 2013). The design specification of FFP normally depends on their applications and project requirements, including its tip geometry (shape and size), instrumentation, mass, and initial impact velocity, as well as soil states (Rong et al. 2024). In terms of soil investigation, various designs have been proposed. Examples include the deep-sea type (>50 kg), such as LIRmeter (Stephan et al. 2012), Deepsea GraviProbe (Lietaert et al. 2016), SeaDart 1 (Peuchen et al. 2017), and lightweight design (≤50 kg), such as the Seabed Terminal Impact Naval Gauge (STING, Mulhearn 2003), Nimrod (Stark et al. 2009), BlueDrop (Stark et al. 2014), and IFFS (Morton et al. 2016). The FFPs used for deep-sea consists of a housing unit that accommodates sensors, a data acquisition system (DAQ), and additional weights. These FFPs have a slender front probe and are about four meters in length with possible extension connections available up to six meters. They weigh over 100 kg and require a relatively large vessel for deployment. Accelerometer(s) are commonly adopted as the main sensor. On the other hand, a lightweight penetrometer weighs below or equal to 50 kg. They consist of shafted, tapered, and full sphere body shapes with similar sensor arrangement as deep-sea penetrometers inside their body void. They can be deployed from a support vessel, or small boats using a winch system or manually dropped from the deck. As the penetrometer falls into the water column, its gravitational potential energy converts to kinetic energy until it impacts the seabed. It reaches the highest velocity/impact velocity upon engagement with the soil material. Subsequently, it begins to decelerate due to counter resistance force applied in the opposite direction, finally coming to rest. The net resistance force, determined by Newton's second law of motion, directly relates to the deceleration. The corresponding static resistance force is calculated by considering the estimated drag force,

buoyant force, submerged weight, and the strain rate effects.

Various techniques have been developed to obtain the soil shear strength from numerous penetrometer systems, including semi-empirical equations (True 1976; Chow and Airey 2014; Chow et al. 2018), analytical models (Dayal 1973; Oliveira et al. 2011; White et al. 2018), and numerical approaches (Zhu and Randolph 2011; Nazem et al. 2012; Moavenian et al. 2016). The interpretation of the FFP test often consists of estimating the static penetration resistance (q_c) according to FFP measured dynamic penetration resistance (q_d) and the strain rate factor (R_f) according to

$$q_c = \frac{q_d}{R_f} \tag{1}$$

The strain rate effect is often known as the increase in penetration resistance with increasing penetration rate and depends on many factors. For clay soil, the strain rate is well established as it is dominated by the soil's vicious effect when penetrating at relatively high rates, and consolidation effects at relatively low rates (Lehane et al. 2009). For sands, recent investigation with constant penetration technique, such as laboratory CPT test, has revealed that the sand rate dependency is predominantly governed by the consolidation effect, as well as by slight compensation arising from viscous rate effects (Chow et al. 2018; 2020). Recent works have provided significant insight into the strain rate effect in the sand but have rarely considered dynamic penetration cases. Due to the increase in nearshore site investigation dominated by sands, there is a need to investigate further into the strain rate effect.

This paper aims to investigate the feasibility study of existing interpretation models for soil characterisation in dynamic penetration cases. A newly developed speargun projectile penetrometer (SPP) has been presented to allow a penetrometer to penetrate uniformly prepared sand beds in a controlled laboratory configuration. The penetration time history data has been recorded to determine the static soil strength by applying the present semi-empirical models. The test result not only demonstrates the penetrability of this deployment method for dynamic penetrometers but also shows the feasibility of some existing models.

2. Strain rate effect models

The rate effect factor (R_f) is the enhanced soil strength measured at a higher loading rate. For sand, the rate effect can be considered as a ratio of sand resistance (q) at a given velocity over the drained resistance (q_{dr}) at the reference velocity. In terms of dilatant sand (dense sand), q/q_{dr} increases with increasing normalised velocity, $V = vd/c_v$, where v is the penetrometer velocity, d is the penetrometer diameter, and c_v is the coefficient of consolidation of soil. A number of studies have looked into the behaviour of normally or lightly over-consolidated clays (Lehane et al. 2009; Nazem et al. 2012; Chow et al. 2014) through normalising the resistance of penetration by a reference undrained resistance.

The rate effect for sand generally can be considered as two parts, including the consolidation rate effect factor ($R_{f.con}$) and the viscous rate effect factor ($R_{f.vis}$). The rate factor in Eq. (1) is defined as

$$R_f = R_{f.con} R_{f.vis} \tag{2}$$

The consolidation rate effect model proposed by Lee and Randolph (2011) and DeJong and Randolph (2012) was then enhanced by Chow et al. (2018; 2020) according to

$$R_{f.con} = \frac{q_{un}}{q_{dr}} + \frac{1 - q_{un}/q_{dr}}{1 + (V/V_{50})^c} \tag{3}$$

where q_{dr} is the reference drained net resistance at $(v/d)_{ref}$, q_{un} is the undrained net resistance at V_{un}, V_{50} is the normalised velocity of 50% consolidation, and c denotes a constant that governs the fitting model curvature change of $R_{f.con}$.

The viscous rate effect has been addressed in recent studies (Chow et al. 2018; 2020). In other studies, while Dayal and Allen (1973) suggested that the viscous rate effect is negligible for sand, White et al. (2018) proposed that nominal undrained shearing may still occur in granular materials. A typical formula for strain rate at a relatively high penetration rate is based on the power law (O'Loughlin et al. 2013) or the Herschel-Bulkley relationship (Zhu and Randolph 2011), respectively represented by

$$R_{f.vis} = \left(\frac{v/d}{(v/d)_{ref}}\right)^{\beta} \tag{4}$$

$$R_{f.vis} = \frac{1 + \mu\left[(v/d)/(v/d)_{ref}\right]^n}{1 + \mu} \tag{5}$$

where v/d is the normalised loading rate, $(v/d)_{ref}$ is the reference loading rate μ defining the viscous property of the sand, and n is the shear-thinning index defining the rate of change of viscosity effect.

The power law is known as the ratio of measured strain rate to reference strain rate to the power of the rate parameter. The Herschel-Bulkley equation is considered through the utilisation of the fluid mechanics model. This approach unveils alterations in the shear zone as the shear-thinning index and Oldroyd number vary, employing large deformation finite element modelling analysis.

The next sections will assess the suitability of the interpretation framework using the results obtained from the speargun projectile penetrometer.

3. Soil sample and preparation

3.1. Soil properties

The silica sand used for this study is a typical river sand with the properties summarised in Table 1. Various soil index tests were conducted according to the relevant standards. Before testing, the specimens were oven dried and kept in moisture contained environment for 48 hours.

Table 1. Silica sand characteristics.

Specify gravity, G_s	2.61
Particle size, d_{50}	425 μm
Minimum density, ρ_{min}	1524.99 kg/m^3
Maximum density, ρ_{max}	1738.02 kg/m^3
Critical friction angle, ϕ'_{cv}	32° (direct shear test)

3.2. Laser displacement sensor

The laser displacement sensor was the primary measurement instrument in this study. It was adopted to monitor the sample settlement during preparation and monitor the speargun projectile penetrometer test. The sensor measurement range was 500 mm. It operated in the principle of optical triangulation, which was a visible, mutilated point of light projected onto the target surface. The distance between the light point on the measuring object and the sensor was calculated by the output signal.

3.3. Vibratory sand compaction

The sand beds were prepared following the technique described by Hariprasad et al. (2016). This technique aims to compact soil to the desired density for the penetration test in a soil container with dimensions of 600×500×700 mm ($L \times W \times H$). The compaction setup is illustrated in Fig 1. The vibration unit was built with plywood and the vibration motor. The vibration motor with 60 W, 50 Hz and 3000 rpm was built into the plywood mould to exert vibration force. A vertical vibration force was applied to the top of the sand. The soil density was controlled using a laser displacement sensor. The sensor monitored the change in height of the vibration unit that reflected the change in soil sample height beneath. The load was applied over a period of approximately two minutes for this test, depending on the final selected density. The sample was saturated after achieving the final density at 20 mm above the soil surface. The final relative density can be simply calculated by knowing the total amount of sand used and the final height, h_s, of the sand specimen.

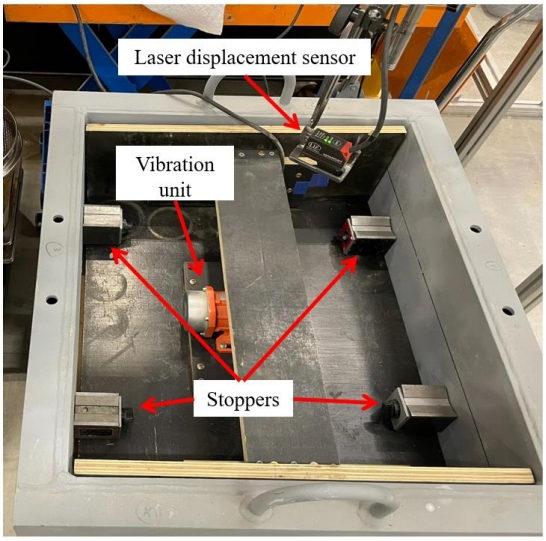

Figure 1. Vibratory compaction set up.

4. Penetrometer test details

This section discusses the speargun projectile penetrometer (SPP) and the test setup. A fully assembled SPP is illustrated in Fig. 2. The test set-up is illustrated in Fig. 3. This schematic model demonstrates the spear at three different times. At the initial state, t_0, the spear is engaged with a speargun and ready to launch, the spear initially impacts the soil sample surface at t_i, and comes to rest at t_f.

4.1. Speargun projectile penetrometer

The speargun projectile penetrometer (SPP) was developed using a speargun gun (see Fig 2). The speargun can generate significant elastic potential energy with the powerband mounted on its rubber muzzle. The powerband can be stretched to 1.2 m, depending on the speargun length, then hooked onto a notch cut on the spear or a small fin. The penetrator is released by pulling the trigger of the speargun. This transfers the elastic potential energy to kinetic energy and allows the spear to launch along the gun barrel rail. It requires a short in-flight distance (h_{if}, see Fig. 3) for the spear to reach its terminal velocity (7 – 30 m/s, with a single powerband) before impacting the specimen. It is worth noting that the in-flight distance is the measured length from the tip to the soil surface at time t_0.

Figure 2. First author with the fully assembled SPP.

In this test, the spears were designed and fabricated in-house. The spear rod, d_{sp}, is 8 mm in diameter, which is smaller than the tip diameter to form a thinly shafted penetrometer. There were four spears made with different notch cut locations to facilitate various powerband stretched lengths. By allowing this, the input energy can be modified based on the test requirement, i.e., the impact velocity is controllable. The speargun for this study is 1.3 m in length. A reflective plate was attached to the spear at 1.4 m from the front to form an object for the laser displacement sensor measurement. For simplicity, this study focuses on a single powerband set-up.

4.2. Laboratory configuration

The test set-up is illustrated in Fig. 3. The spear was launched from the speargun mounted to a working platform with a launch mechanism. A launch mechanism includes a steel frame installed on a working platform to secure the speargun. It is designed for two main purposes. The first purpose is to accommodate the instrumentations and the SPP for safely launching from behind the working platform and provide repeatability for testing, i.e. achieving the same in-flight distance, h_{if}, and soil height, h_s. Second, the launch mechanism was developed to investigate its applicability as a survey ship accessory mounted to the ship side for launching the SPP for future experiments and applications.

The laser displacement sensor is attached to the launch mechanism at a certain position to capture the displacement time profile of the spear from t_i to t_f. The sensor should be located at 600 mm plus h_{if} from the reflective plate.

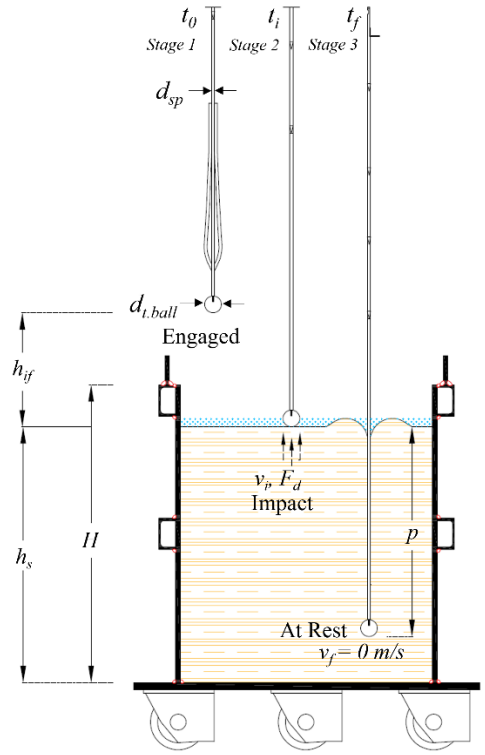

Figure 3. Test set-up and scheme.

4.3. Operation procedures

The testing protocol was established to ensure consistent operations in the following manner for reputability as follow:

1. Spear assembly: The operator selects the spear tip and assembles the spear by securely attaching the tip and reflective plate;
2. Sensor set-up: For the laser displacement sensor, installation is crucial; it should be positioned at the designed height from the soil surface and aligned with the reflective plate. In this study, the in-flight distance after being launched from the speargun was set at 400 mm to allow ample space for the penetrometer to reach its terminal velocity. Simultaneously, the sensor was positioned at 1000 mm from the reflective plate;
3. Loading speargun: The fully assembled penetrometer is loaded onto the speargun, ensuring that the safety catch is engaged;
4. Powerband attachment: The powerband is tethered to the notch cut on the spear, followed by unlocking the safety catch. Subsequently, data acquisition on the control computer commences;
5. Data acquisition: The test is initiated by pulling the trigger and launching the spear. Once the spear comes to rest, data acquisition is halted, and recordings are downloaded. Concurrently, the penetrometer's embedment depth is directly measured using a ruler;

5. Test results

5.1. Embedment depth

The test data is summarised in Table 2. Three tests are selected for interpretation discussion with equal input energy during launching, i.e., the speargun powerband stretched length is the same at x = 400 mm. The kinetic energy at t_i is about 99 – 100 J, depending on the mass which slightly varies with the tip size. The final density measured after vibratory compaction is reasonably close to 80%, representing dense sand. The ball diameter in tests A1 and A2 is 20 mm, whereas it is 35 mm in test A3. There tests were conducted from two different sand beds.

Table 2. SPP test results.

Test	x_{pb} (mm)	$d_{t.ball}$ (mm)	p/d (mm)	v_i (m/s)	D_r
A1	400	20	20.21	12.00	80.2%
A2	400	20	19.60	11.10	77.0%
A3	400	35	4.62	12.02	77.1%

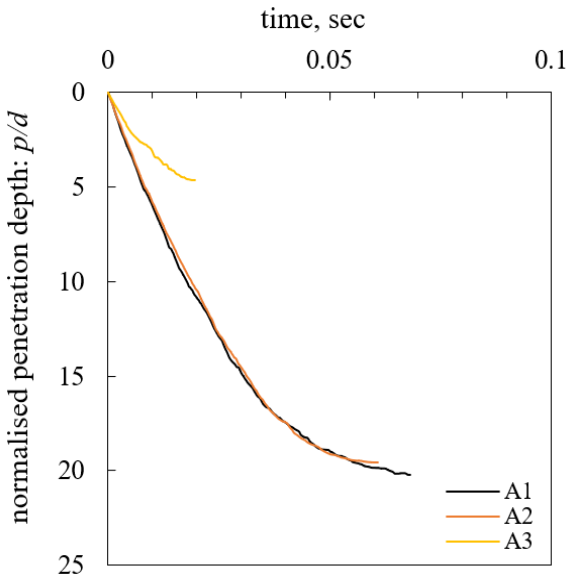

Figure 4. Normalised penetration(p/d) versus time.

Fig. 4 plots the penetration normalised by diameter, p/d, versus time (s). The final normalised embedment depth achieved by the 20 mm ball is 20.2, which is much higher than its counterpart obtained by the 35 mm ball.

5.2. Dynamic penetration resistance, q_d

The acceleration profile can be obtained by double numerical differentiation of the displacement versus time. The dynamic penetration resistance force, F_d, can then be calculated using Newton's second law of motion ($ma = W - F_d$). Finally, the dynamic penetration resistance, q_d, is obtained by dividing F_d by the projected tip area, $A = \pi d_t^2/4$, where d_t is the projected tip diameter. The shaft (sleeve) friction in the tests is neglected because the rod diameter is smaller than the tip diameter. The assumption of ignoring shaft friction F_s, is supported by field tests conducted by the STING and model FFP (Mulhearn 2003). In addition, the drag forces F_D may also be ignored due to the low water depth. This approach is similar to a model FFP test interpretation proposed by Chow and Airey (2013).

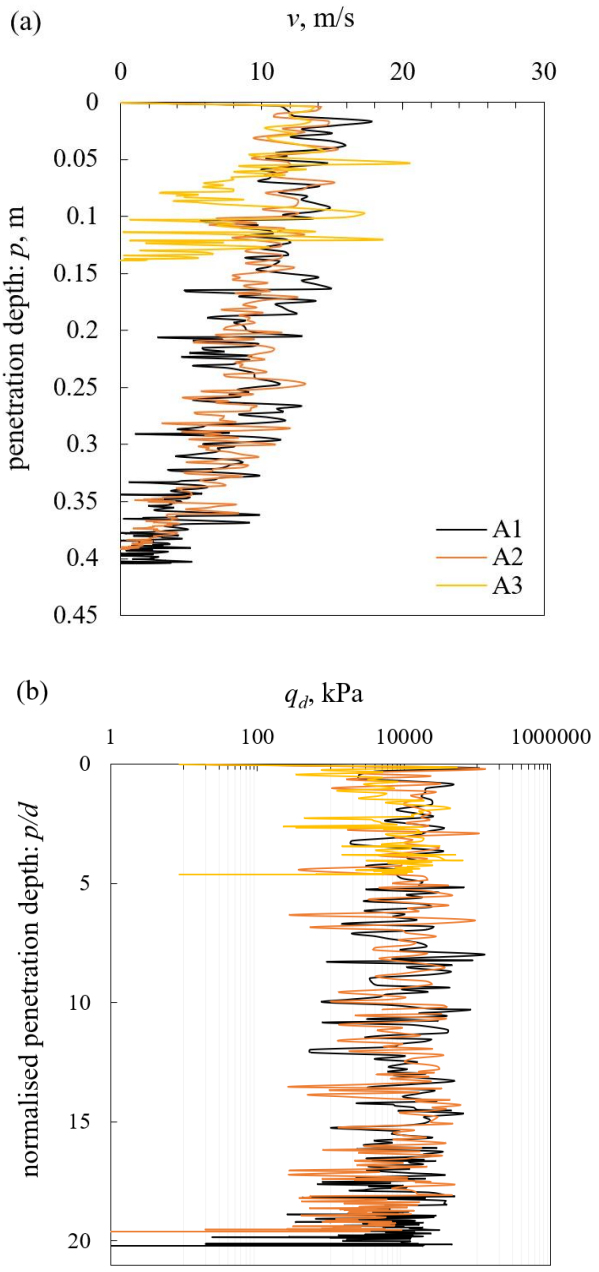

Figure 5. Test result, (a) velocity profile of SPP tests; (b) repeatability of SPP (v_i = 11.5 m/s, $d_{t,ball}$ = 20 mm, D_r = 77%).

Typical profiles of q_d and the corresponding velocity versus penetration depth from three SPP tests into the same sand bed are shown in Fig. 5. The test results in Fig. 5.a with similar final depths and resistances indicate the repeatability of the test data as well as the uniformity of the sand bed strength prepared using the vibratory compaction approach.

The dependency of the strain rate effect factor, R_f, is associated with the normalised velocity, which governs the consolidation rate effect. The model is also known to be a 'backbone curve' framework in relation to the effect of drainage conditions during penetration. As the normalised velocity increases, the soil behaviour undergoes a transition from drained to partially drained, and eventually to undrained conditions. The proposed transition boundary is that the condition for fully drained response has been established as $V_{dr} < 0.3$ and the undrained condition, $V_{un} > 30$ in normally consolidated clay (DeJong and Randolph 2012; Chow et al. 2018, 2022).

To investigate the drainage condition of the SPP test, Fig. 6 illustrates a typical range of the normalised velocity of SPP tests versus normalised penetration depth, p/d. The penetrometer was recorded to impact the soil with V = 1200 to 1300. The value of V in tests A1 and A2 began to decline beyond p/d = 15, whereas A3 decreased rapidly after reaching p/d = 3. All test results indicate that the drainage conditions are largely above the proposed undrained threshold.

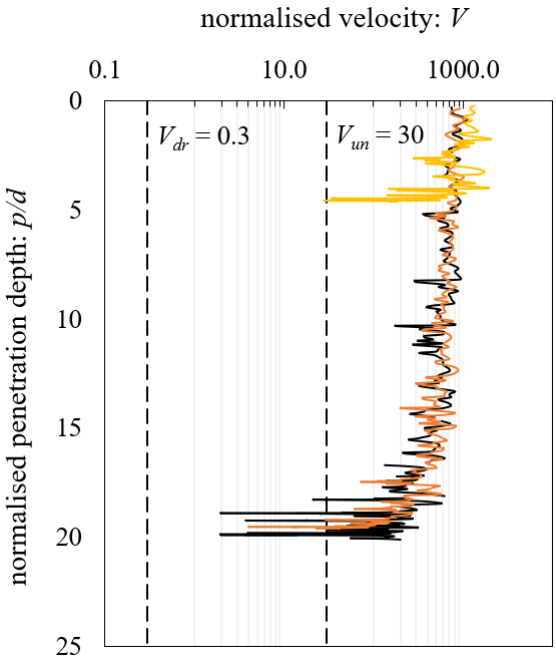

Figure 6. Normalised velocity versus p/d of SPP tests.

6. Determination of the static penetration resistance

A model to estimate the undrained resistance of sand was proposed by Bolton (1986), who investigated data produced by triaxial tests with 17 different types of sands and provided a correlation between density friction angle and dilation angle, varying with effective stress level. By understanding that in undrained failure the dilation angle must be zero, Bolton's proposed relationship can be used

to estimate the undrained shear resistance of sand according to

$$q_{un} = \frac{1}{2} e^{Q-1/D_r} \left(\frac{6 \sin \phi_{cv}}{3 - \sin \phi_{cv}} \right) N_{kt} \qquad (6)$$

where *Dr* is the relative density of sand; *Q* is the crushing strength parameter, taken as 10 for silica sand, and ϕ_{cv} is the friction angle. As suggested in White et al. (2018) and Zhu and Randolph (2009), the N_{kt} is between 12 to 15. The highest value of N_{kt} of 15 is for the ball tip, but it is affected by a shallow embedment when the penetration depth is relatively low. By substituting the friction angle and relative density into the model, an analytical static penetration resistance can be obtained.

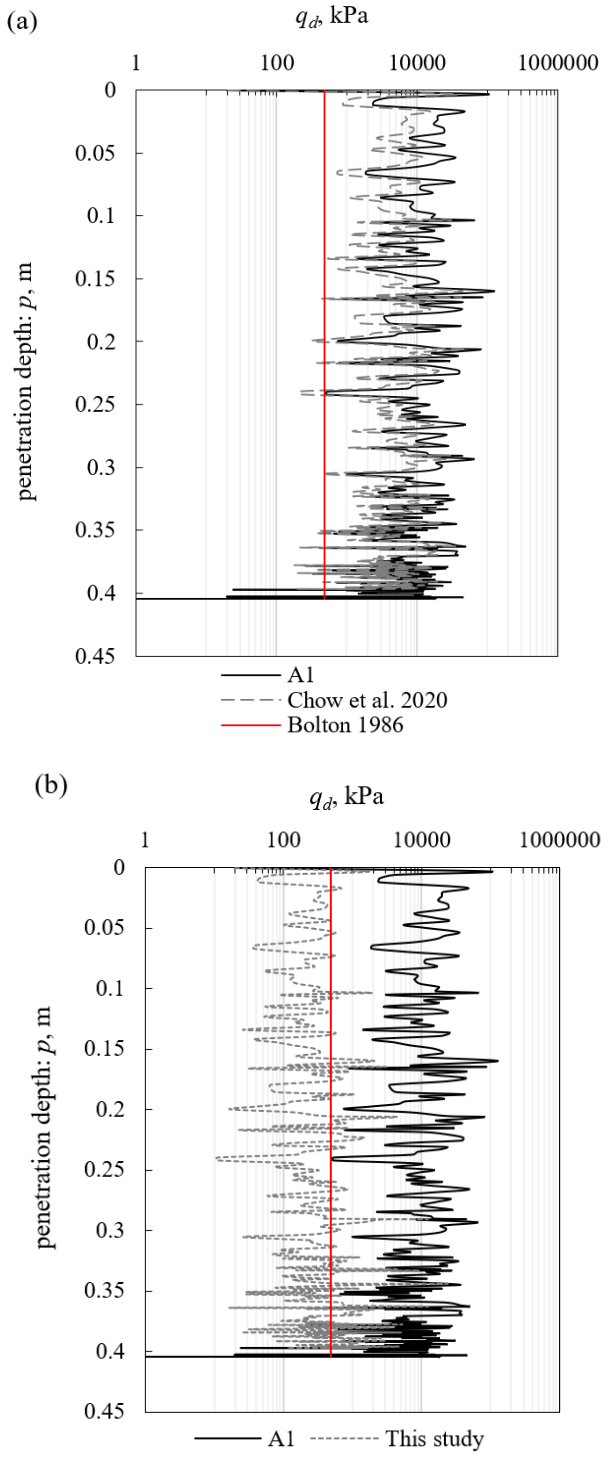

Figure 7. determination of q_c for various tests using different parameters.

In order to determine the static penetration resistance, the rate effect model, Eq. (2), was substituted into Eq. (1) with the consolidation effect given by Eq. (3), and viscous effect by Eq. (4) or (5). According to Chow et al. (2018), the strain rate effect model employed for the CPTu test showed a reasonably good fit for dense sand material. Chow et al. (2020) suggested the following parameter for piezocone: q_{un}/q_{dr} = 4, V_{50} = 3000, c = 1.3, μ = 0.35, v_{ref} = 0.0006 m/s, and n = 0.075, with the Herschel-Bulkley model adopted for viscous effect. The same fitting parameters were applied for the SPP, and the result is shown in Fig. 7.a This yields a value of R_f = 3 in average, resulting in a significantly higher q_c compared to the reference value estimated using Bolton's model. This might be due to the significantly higher impact velocity adopted in this test leading to greater rate effect.

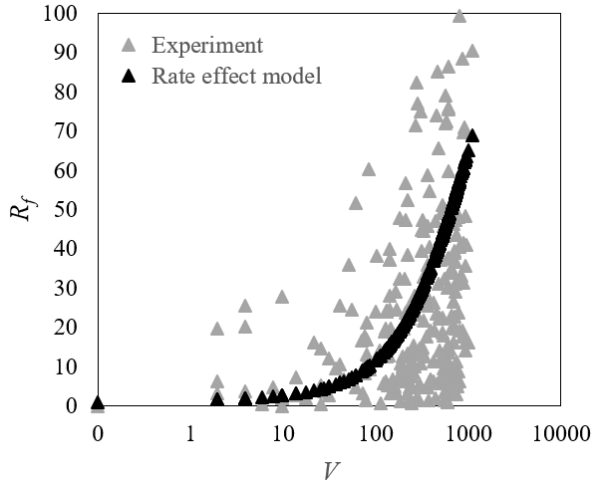

Figure 8. Normalised velocity versus R_f for A1.

Another set of parameters was applied to determine the rate factor in order to characterise the best-fit model for the corresponding q_c. They include q_{un}/q_{dr} = 15, V_{50} = 750, c = 1.5, μ = 0.3, and n = 0.3. The result of q_c for the SPP tests is shown in Fig. 7.b, 7.c and 7.d. This set of parameters provides a reasonable fit to the experimental data versus Bolton's solution, regardless of the tip size. This is demonstrated in Fig. 7.d by applying the same fitting parameters for A3 with a 30 mm tip. Meanwhile, the normalised velocity is plotted versus the rate factor for test A1 in Fig. 8. The model showed an increase in Rf with increasing V, aligning with the proposed 'backbone curve' in Chow et al. (2018) for dense sand. Similar results were also obtained for tests A2 and A3. It is notable that modifying the viscous rate effect parameter considerably changes the fitting curve. This indicates that the viscous effect could be present under a high loading rate.

6.1. Viscous rate effect

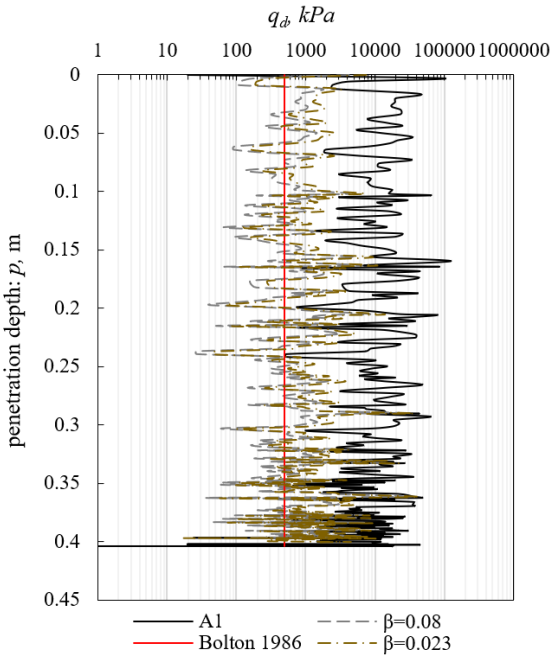

Figure 9. Viscous rate effect model fitting with different rate parameter

While viscous rate effects in sand are typically considered secondary in comparison to consolidation, they have been reported to result in approximately a 10% increase in shear strength per logarithmic cycle rise in strain rate (Dayal and Allen 1975). To study the viscous rate effect, the Herschel-Bulkley equation is replaced by the power-law to fit test A1 with different rate parameters, β. Meanwhile, the consolidation effect remains being modelled using Eq. (3) with q_{un}/q_{dr} = 15, V_{50} = 750, c = 1.5.

A rate parameter of β = 0.09 is known as a typical value used in FFP field tests and anchor installation (O'Loughlin et al. 2013; Morton et al. 2016; Chow et al. 2019). For β = 0.09, the average q_c is 7% higher than the average q_c when the rate parameter is 0.08. Fig. 9 plots the dynamic resistance versus the penetration assuming rate parameters β = 0.023 and 0.08. For β = 0.023 the average q_c is 60% higher than its counterpart for β = 0.08. The resulting q_c curve has changed slightly due to this modification in the rate parameter. This indicates that the viscous rate effect in the recently proposed equation can be adopted for determining the static penetration resistance from dynamic resistance records. It also suggests the potential of a fluid-like behaviour of sand under undrained conditions. Future studies with higher impact velocities are required to further investigate and understand this phenomenon.

7. Conclusion

This study investigated the feasibility of a speargun projectile penetrometer (SPP) test to assess the properties of sandy sediments, focusing on the strain rate effects arising from consolidation and viscous rate effects in dense sand samples. The laboratory test set-up allows the speargun to launch a penetrometer to a homogeneous sand sample prepared using the vibratory method. The penetration and time are captured with a laser displacement sensor. The final embedment result showed that the SPP launch with external energy input can achieve high penetration depths in comparison to free-falling penetrometers. The test results revealed that the undrained conditions for sand were achieved as V is considered to mostly remain above the undrained regime. Studying the significant rate effects in sands is crucial due to the growing need for offshore green energy production in shallow waters predominantly filled with sandy material.

The rate dependency of sand was examined using the SPP data with the application of the existing strain rate effect model. For reference, the soil static resistance was determined utilising the strain rate correction based on Bolton's equation. The rate effect model proposed by Chow et al. (2018; 2020) demonstrated a good fit to the experimental data. However, it is important to note that the uncertainty in this research is associated with certain parameter selections for data fitting and the reference resistance model. To address this, further investigation can be conducted with both higher and lower penetration rates in the sand, as well as a constant rate penetration test, involving additional experiments with constant rate penetration to refine the model. Moreover, exploring the

application of the model in dynamic cases within the backbone framework demands further study.

Acknowledgement

This project is financially supported by the Australian Research Council through the Discovery Project scheme (DP200100549). This support is greatly acknowledged.

Reference

Bolton, M.D., 1986. "The strength and dilatancy of sands". *Géotechnique*, 36(1), pp.65-78. https://doi.org/10.1680/geot.1987.37.2.219.

Chow, S.H. and Airey, D.W., 2013. "Soil strength characterisation using free-falling penetrometers". *Géotechnique*, 63(13), 1131-1143. https://doi.org/10.1680/geot.12.P.129.

Chow, S.H. and Airey, D.W., 2014. "Free-Falling Penetrometers: A Laboratory Investigation in Clay". *Journal of Geotechnical and Geoenvironmental Engineering*, 140(1), 201-214. https://doi.org/10.1061/(ASCE) GT.1943-5606.0000973.

Chow, S.H., Bienen, B. and Randolph, M.F., 2018. Rapid penetration of piezocones in sand. In: *Cone penetration testing 2018*. pp. 213-219.

Chow, S.H., Bienen, B. and Randolph, M.F., 2020. "Rapid penetration of spudcans in sand". In: *4th International Symposium on Frontiers in Offshore Geotechnics*. pp. 2238-2247.

Chow, S.H., Bienen, B., Randolph, M. and Roy, A., 2022. "Rapid soil-structure interactions in saturated sand." In: *20th International Conference on Soil Mechanics and Geotechnical Engineering*. Sydney, Australia, pp 2615 – 2620.

Chow, S.H., O′ Loughlin, C.D., and Randolph, M.F., 2014. "Soil strength estimation and pore pressure dissipation for free-fall piezocone in soft clay." *Géotechnique* 64 (10), 817–827. https://doi.org/10.1680/geot.14.P.107.

Chow, S.H., Verth, A., Zang, L., Orszaghova, J., Bradley, R., Wolgamot, H. and Beemer, R., 2019. "Mooring of wave energy system using dynamically installed anchors." In: *Proceedings of the AGS international 13th Australia New Zealand Conference on Geomechanics*. Sydney, Australia, pp. 679-684.

Dayal, U. and Allen, J.H., 1973. "Instrumented impact cone penetrometer." *Canadian Geotechnical Journal*, 10(3), 397-409. https://doi.org/10.1139/t73-034

DeJong, J.T. and Randolph, M., 2012. "Influence of partial consolidation during cone penetration on estimated soil behavior type and pore pressure dissipation measurements." *Journal of Geotechnical and Geoenvironmental Engineering*, 138(7), 777-788. https://doi.org/10.1061/(ASCE)GT.1943-5606.0000646.

Lee, J. and Randolph, M., 2011. "Penetrometer-based assessment of spudcan penetration resistance." *Journal of geotechnical and geoenvironmental engineering*, 137(6), 587-596. https://doi.org/10.1061/(ASCE)GT.1943-5606.0000469

Lehane, B.M., O'Loughlin, C.D., Gaudin, C. and Randolph, M.F., 2009. "Rate effects on penetrometer resistance in kaolin." *Géotechnique*, 59(1), 41-52. https://doi.org/10.1680/geot.2007.00072.

Lietaert B., Charlet F. and Staelens P., 2016. "Geotechnical Characterization of Very Soft Deep-Sea Sediments by In-Situ Penetrometer Testing." In: *Proceedings of 25th European Young Geotechnical Engineers Conference*. Sibiu, Romania, pp 61-72.

Moavenian, M.H., Nazem, M., Carter, J.P. and Randolph, M.F., 2016. "Numerical analysis of penetrometers free-falling into soil with shear strength increasing linearly with depth." *Computers and Geotechnics*, 72, 57-66. https://doi.org/10.1016/j.compgeo.2015.11.002.

Morton, J.P., O'Loughlin, C.D. and White, D.J., 2016. "Estimation of soil strength in fine-grained soils by instrumented free-fall sphere tests." *Géotechnique*, 66(12), 959-968. https://doi.org/10.1680/jgeot.15.P.038.

Mulhearn, P. J., 2003. "Influences of penetrometer tip geometry on bearing strength estimates." *International Journal of Offshore and Polar Engineering*, 13(1), 73–78.

Nazem, M., Carter, J.P., Airey, D.W., and Chow, S.H., 2012. "Dynamic analysis of a smooth penetrometer free-falling into uniform clay." *Géotechnique*, 62 (10), 893–905. https://doi.org/10.1680/geot.10.P.055.

O'Loughlin, C.D., Richardson, M.D., Randolph, M.F., and Gaudin, C., 2013. "Penetration of dynamically installed anchors in clay." *Géotechnique* 63(11), 909–919. https://doi.org/10.1680/geot.11.P.137.

Oliveira, J.R., Almeida, M.S., Motta, H.P. and Almeida, M.C., 2011. "Influence of penetration rate on penetrometer resistance." *Journal of Geotechnical and Geoenvironmental Engineering*, 137(7), 695-703. https://doi.org/10.1061/(ASCE)GT.1943-5606.0000480.

Peuchen, J., Looijen, P.N. and Stark, N., 2017. "Offshore characterisation of extremely soft sediments by free fall penetrometer." In: *Proceedings of the 8th Offshore Site Investigation and Geotechnics International Conference*. United Kingdom, London, pp. 370-377. https://doi.org/10.3723/OSIG17.370.

Rong, J., Nazem, M., Chow, S.H., Zhou, A. and Moridpour, S., 2024. "Design and application of dynamic seabed penetrators in offshore geotechnical engineering: A review." *Ocean Engineering*, 293, 116599. https://doi.org/10.1016/j.oceaneng.2023.116599.

Stark, N., Hay A. E. and Trowse G., 2014. "Cost-effective geotechnical and sedimentological early site assessment for ocean renewable energies." *Oceans - St. John's*, pp. 1-8. https://doi.org/10.1109/OCEANS.2014.7003004.

Stephan, S., Kaul, N. and Villinger, H., 2012. "The Lance Insertion Retardation meter (LIRmeter): an instrument for in situ determination of sea floor properties—technical description and performance evaluation." *Marine Geophysical Research*, 33(3), 209-221. https://doi.org/10.1007/s11001-012-9156-2.

True, D. G., 1976. "Undrained vertical penetration into ocean bottom soils." *PhD thesis*, University of California, Berkeley.

White, D.J., O'Loughlin, C.D., Stark, N. and Chow, S.H., 2018. "Free fall penetrometer tests in sand: Determining the equivalent static resistance." In: *Proceedings of the 4th International Symposium on Cone Penetration Testing*. Delft, Netherlands, pp. 695-701.

Zhou, H. and Randolph, M.F., 2009. "Resistance of full-flow penetrometers in rate-dependent and strain-softening clay." *Géotechnique*, 59(2), 79-86. https://doi.org/10.1680/geot.2007.00164.

Zhu, H. and Randolph, M.F., 2011. "Numerical analysis of a cylinder moving through rate-dependent undrained soil." *Ocean Engineering*, 38(7), 943-953. https://doi.org/10.1016/j.oceaneng.2010.08.005.